ADVANCED FUNCTIONAL MATERIALS
www.afm-journal.de

Rapid Regeneration of Graphite Anodes via Self-Induced Microwave Plasma

Minghui Shan, Shuchang Xu, Yunteng Cao, Bing Han, Xiaoqing Zhu, Tao Zhang, Chenyang Dang, Jiacheng Zhu, Qi Zhou, Zhixin Xue, Yaping Xu, Qixuan Zhu, Md Shariful Islam, Ben Hang Yin, Xijiang Chang, Changyong (Chase) Cao, Guiyin Xu,* and Meifang Zhu*

Battery recycling is a promising approach to mitigate the safety, environmental, and economic threats posed by numerous discarded lithium-ion batteries (LIBs). However, the unclear atomic-scale degradation of spent graphite complicates recycling, resulting in energy-intensive impurity removal and graphitization, which hampers industrialization. This study uses Cryo-transmission electron microscopy (Cryo-TEM) to characterize spent graphite degradation and develop a scalable graphite self-induced microwave plasma method for efficient regeneration. Cryo-TEM images show graphite coated with a solid electrolyte interphase (SEI) layer, revealing lattice defects and structure expansion near the surface that impair electrochemical performance. The self-induced microwave plasma method eradicates the SEI layer and restores the graphite lattice structure within 30 s. Multiphysics simulations indicate that the microwave field generates a strong electric field on the graphite surface, causing plasma discharge and rapid surface heating. Regenerated graphite demonstrates excellent electrochemical performance, with a specific charge capacity of 352.2 mAh g^{-1} at 0.2 C and ≈81% capacity retention after 400 cycles, matching commercially available materials. This efficient method offers a promising approach for recycling graphite anodes.

1. Introduction

Lithium-ion batteries (LIBs), valued for their high energy density, long cycle life, portability, and environmental benefits, are widely used in energy storage and electric vehicles.[1–4] However, many are approaching their average lifespan of 8–10 years.[5–8] By 2025, retired batteries are expected to total 120 GWh.[9] Improper disposal, such as landfills or incineration, can release toxic components, causing severe environmental pollution.[10,11] Consequently, battery recycling is increasingly recognized as an effective strategy to mitigate the environmental impact of spent batteries[12] The principle of atom economy in resource management highlights the environmental benefits of recycling spent LIBs.[13] Reusing recycled materials from retired batteries holds significant potential for establishing an industrial closed-loop, offering economic advantages in the battery manufacturing

M. Shan, X. Zhu, T. Zhang, C. Dang, J. Zhu, Z. Xue, Y. Xu, Q. Zhu, G. Xu, M. Zhu
State Key Laboratory for Modification of Chemical Fibers and Polymer Materials and College of Materials Science and Engineering
Donghua University
Shanghai 201620, China
E-mail: xuguiyin@dhu.edu.cn

S. Xu, Q. Zhou, X. Chang
College of Science
Donghua University
North Renmin Road 2999, Shanghai 201620, China

The ORCID identification number(s) for the author(s) of this article can be found under https://doi.org/10.1002/adfm.202411834

DOI: 10.1002/adfm.202411834

Y. Cao
Department of Civil and Environmental Engineering
Massachusetts Institute of Technology
Cambridge, MA 02139, USA

B. Han
Eastern Institute for Advanced Study
Eastern Institute of Technology
Ningbo, Zhejiang 315200, China

M. S. Islam, C. (Chase) Cao
Laboratory for Soft Machines & Electronics
Department of Mechanical and Aerospace Engineering
Case Western Reserve University
Cleveland, OH 44106, USA
E-mail: ccao@case.edu

B. H. Yin
Paihau-Robinson Research Institute and the MacDiarmid Institute for Advanced Materials and Nanotechnology
Victoria University of Wellington
Wellington 6012, New Zealand

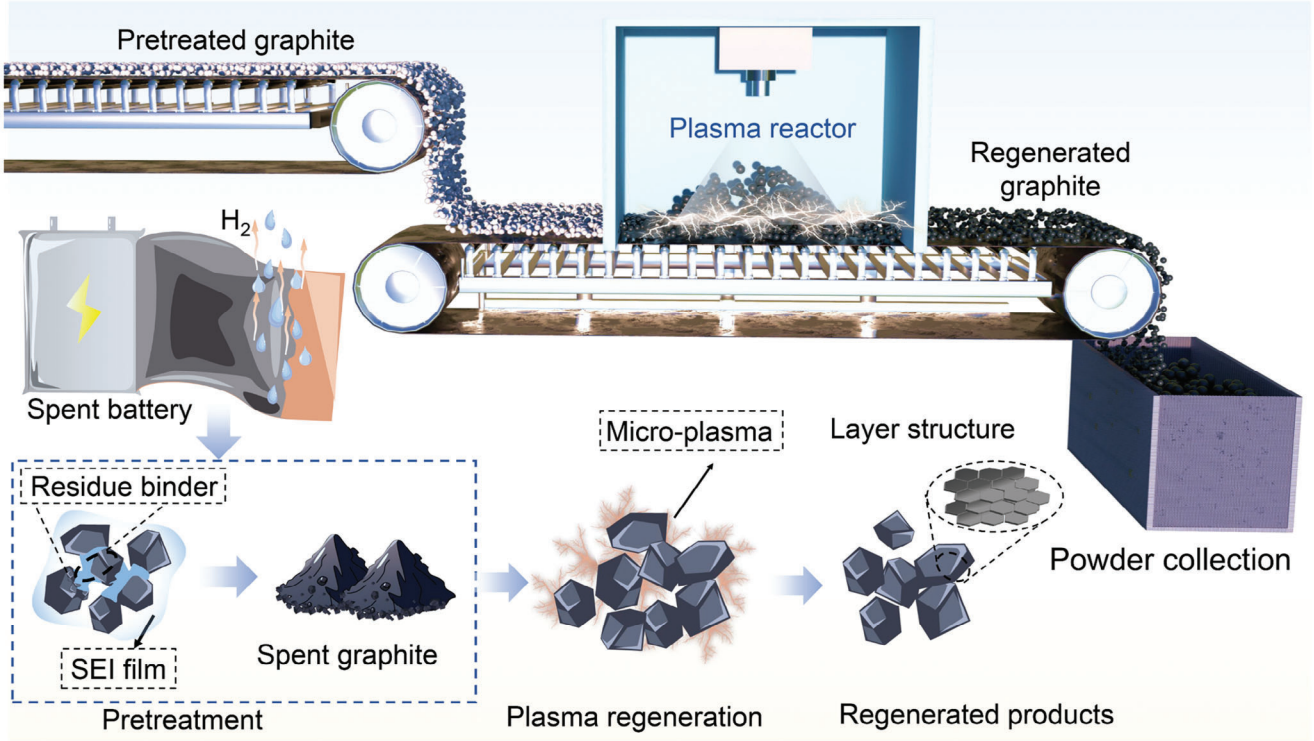

Figure 1. Schematic illustration of the regeneration process and mechanism for graphite anodes using a novel graphite self-induced microwave plasma (GMP) method. In the microwave field, graphite induces plasma around its surface, generating intense thermal effects that remove the SEI layer and residual binder, and repair the graphitization of spent graphite. It can be used for scalable continuous regeneration of graphite anodes.

industry.[14,15] Graphite, as the anode material, accounts for ≈20% of the total mass and 10% of the total cost of batteries.[16–18] However, compared to cathode recycling, graphite recycling has been overlooked due to low margins and technical challenges, such as harsh recycling conditions, poor performance, and scalability issues.

Currently, graphite anodes are recycled using standard industrial practices such as hydrometallurgical and pyrometallurgical methods, primarily to recover metals from electrode materials.[19,20] For example, impurities on the surface of graphite anode are removed by acid/alkali leaching in hydrometallurgical methods,[20–22] while the pyrometallurgical process calcinates the graphite anodes with cathode materials. However, the extensive use of strong acids/alkalis and the energy-intensive calcination over extended periods harms the environment and sustainability and degrades the quality of recycled graphite, making it difficult to meet reuse standards. Therefore, it is highly desired to explore effective and sustainable processes to recycle spent graphite.

Recent efforts have shown that the performance gap between spent and commercial graphite is attributed to the thick passivation layer, metal impurities, organic binder, and structural defects in graphite.[23,24] These defects could be repaired by direct regeneration methods after rapid stripping and post-treatment.[25–28] For example, Zhou et al.,[29] proposed a novel closed-loop recycling method that leveraged residual lithium metal produced during cycling to separate graphite scrap from copper foils and harvest lithium for replenishment and cathode material synthesis. Additionally, a flash Joule heating method was proposed to remove binders,[30] residual solid electrolyte interphase (SEI) layers, and rapidly repair the structural defects.[31,32] Despite these advances, detailed degradation analysis, such as lattice defect distribution and SEI thickness after cycling, have not been conducted, leading to extensive energy consumption for graphite repair and impeding targeted regeneration technology development.

Herein, we analyzed the degradation mechanism of spent graphite using Cryo-transmission electron microscopy (Cryo-TEM). Cryo-TEM images showed the layered graphite lattices coated with a nano SEI layer, with lattice defects and structure expansion near the surface, indicating structure damage during battery cycling. The thick and uneven SEI layer, composed of inorganic nanocrystals and organic amorphous components, impairs capacity and rate capability. Based on these findings, we developed an innovative graphite self-induced microwave plasma (GMP) method for efficient, scalable regeneration of spent graphite. In the microwave field, graphite induces plasma around its surface (Plasma regeneration in **Figure 1**), generating intense thermal effects[33] that remove the SEI layer and residual binder, and repair the graphitization of spent graphite in just 30 s. Multiphysics simulations showed that the microwave field induces an electric field around graphite particles, causing plasma discharge and high temperatures that remove impurities and repair the structure. The regenerated graphite exhibited excellent electrochemical performance with a specific charge capacity of 352.2 mAh g^{-1} at 0.2 C and ≈81% capacity retention after 400 cycles, comparable to commercially available fresh materials. Additionally, a specialized device was designed for continuous plasma regeneration of spent graphite anode materials (Figure 1),

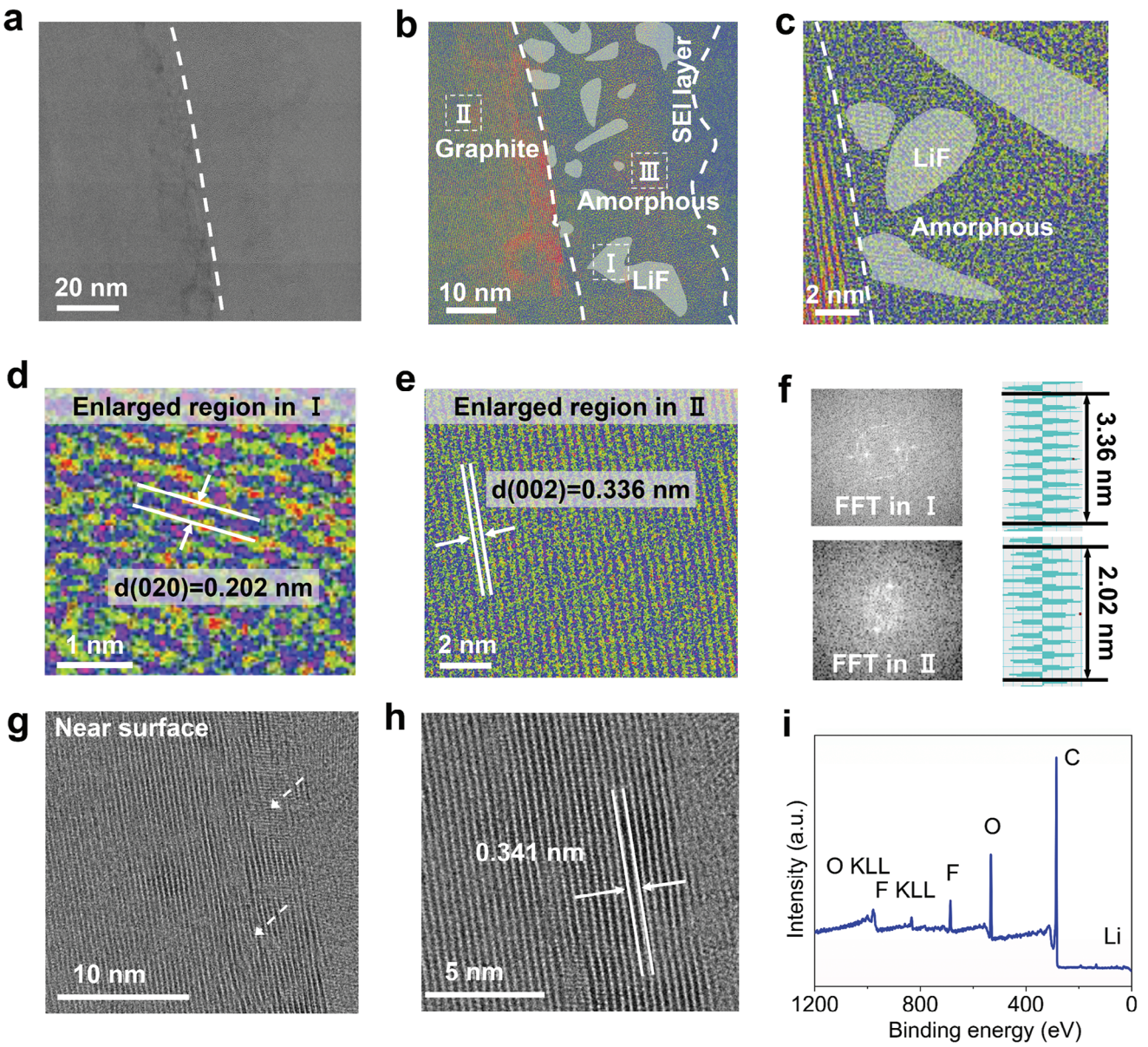

Figure 2. Characterization of the graphite anodes in spent batteries. a–e) Cryo-HRTEM images of spent graphite particles and zoom-in images of d) region I and e) region II. f) Fast Fourier Transform (FFT) of regions I and II. g) Cyro-HRTEM images of structure defects and (h) lattice expansion of spent graphite i) XPS full-spectrum of spent graphite. Note: color does not represent any information in (b–e).

indicating the potential of the new method for scalable and practical applications.

2. Results and Discussion

2.1. Degradation Analysis of Graphite Anodes in Spent Batteries

The battery experiences capacity decay after long-term cycling in various conditions, primarily due to the loss of active lithium and damage to the electrode lattice.[23,34] For example, the formation of SEI and the growth of lithium dendrite consume active lithium at the anode. These side reactions increase impedance, hinder lithium-ion transport, and lead to more serious side reactions and potential battery failure. Therefore, detailed research into the degradation mechanism is crucial. Known degradation mechanisms include thick SEI formation, lithium dendrite growth, and volume expansion during cycling.[35]

In this section, Cryo-TEM and Cryo-High Resolution Transmission Electron Microscopy (Cryo-HRTEM) were employed to characterize graphite particles collected from spent batteries at the atomic scale, revealing the detailed degradation conditions. Cryo-TEM images showed an uneven SEI layer of ≈40 nm formed on the surface of graphite particles (**Figure 2a**; Figure S1 and S2a, Supporting Information). This SEI layer consists of an amorphous region and nanocrystals, coincident with previous reports.[36] The nanocrystals are dispersed within the amorphous

phase, with lattice spacings of 0.20 and 0.27 nm, corresponding to the (020) and (111) crystallographic planes of LiF and Li_2O, respectively (Figure 2a–c,f). These components align with the SEI layer formed in EC, DEC, and FEC electrolytes,[36] with LiF being the main inorganic component. Despite the formation of the SEI layer, atomic-resolution images revealed that graphite particles retained their layered lattice structure, confirmed by the 0.336 nm lattice spacing of region II, corresponding to the (002) crystallographic plane of graphite (Figure 2e,f). However, the lattice damage appeared near the surface of the graphite (Figure 2g). Defects and a discontinuous layer structure were evident, as shown by split spots in HRTEM and inverse Fast Fourier Transform (FFT) images (Figure S3, Supporting Information). Additionally, the graphite layer near the surface exhibited a bigger interlayer spacing of 0.341 nm (Figure 2h; Figure S4a–c, Supporting Information) compared to the bulk phase. These findings indicate the deterioration of crystal structure during the intercalation and deintercalation of lithium ions.

Electron diffractogram patterns of scrap graphite in selected regions further verified the crystal structures of graphite and LiF (Figure S5, Supporting Information). X-ray photoelectron spectroscopy (XPS) was used to further characterize the SEI components on the surface of spent graphite (Figure 2i, Supporting Information). The C 1s peaks (Figure S6, Supporting Information) indicate bonds primarily consisting of C—C, C—O, C—H, C═O, O—C—F, and O—C—O, corresponding to the organic components and carbonate products of the electrolyte and SEI layer.[31] Fitting its F 1s to Li 1s (Figure S7, Supporting Information), the metal fluoride peaks further indicated the presence of LiF, consistent with Cryo-HRTEM results. Thermogravimetric Analysis (TGA) showed that inorganic LiF has high chemical stability (Figure S8, Supporting Information),[37] indicating the formation of a thick and uneven SEI layer composed of dispersed crystalline LiF and Li_2O and compact amorphous regions on graphite particles, reflecting electrolyte decomposition during cycling.[38] The Raman spectrum (Figure S9, Supporting Information) of spent graphite anode (SG) shows a high I_D: I_G value of 0.77, indicating the low graphitization degree and the deterioration of the graphite structure. XRD spectrum (Figure S10, Supporting Information) of SG without leaching demonstrates some impurities in SG with a slight signal, which may be caused by the existing lithium salt.

While the SEI layer maintains structural integrity and ion transport, it consumes active lithium and reduces direct contact between graphite particles and electrolytes, increasing impedance and causing capacity degradation.[36,39] Lattice deterioration and reduced graphitization also harm the electrochemical performance of graphite anodes. The performance impacts of these degradation modes were further investigated. Specific discharge capacities of half-cells assembled with spent graphite at 0.1, 0.2, 0.5, 1, and 2 C were 297.78, 251.82, 168.20, 49.16, and 7.44 mAh g^{-1}, respectively (Figure S11, Supporting Information), significantly lower than the theoretical capacity of graphite (372 mAh g^{-1}).[40] Spent graphite anodes also presented poor rate capability, with substantial capacity attenuation at 2 C. Coulombic efficiencies of charge and discharge at 0.1, 0.2, 0.5, 1, and 2 C were 87.74%, 99.45%, 99.58%, 97.86%, and 69.45%, respectively (Figure S12, Supporting Information), confirming the ion transport impedance caused by the SEI layer. The initial Coulombic efficiency of the spent graphite was lower than 90%, indicating the formation of a new SEI layer on the graphite surface. At 1 and 2 C, Coulombic efficiencies were lower than the lithium deposition threshold of 97%–98%, leading to a thicker SEI.[41,42] Additionally, if deposited lithium metal is shed, it can react with the electrolyte to form an SEI layer wrapped in dead lithium, further depleting active lithium.[43,44] Therefore, spent graphite anodes do not meet the criteria of reutilization in commercial batteries, underscoring the necessity of regeneration to enhance electrochemical performance.

2.2. Regeneration of Graphite Anodes

The degradation of graphite anodes is primarily due to the thick SEI layer on the surface and damage to the crystal lattice near the surface, resulting in high impedance and sluggish Li^+ insertion during battery cycling (**Figure 3a**). Therefore, it is imperative to remove the residual SEI layer and repair the graphite layer. After mechanically disassembling spent batteries, we obtained electrode sheets composed of copper foil and spent graphite anode (Figure S13, Supporting Information). These electrode sheets underwent ultrasonic stripping in a water-ethanol solution to leach the graphite and eliminate surface impurities. The lithium metal in the graphite sheets reacted with the leaching solution, generating hydrogen gas (Figure S14, Supporting Information).[29,45] This process could completely detach SG from the copper foil (Figure S15, Supporting Information), suspending the SG in the solution. After separation, the leached graphite anode (LG) was treated with GMP for 10, 20, and 30 s under a nitrogen atmosphere for regeneration (Figure S16, Supporting Information). The graphite anode treated for 30 s showed a high specific charge capacity at 0.05 C (Figure S17, Supporting Information), comparable to the theoretical capacity.

X-ray diffraction (XRD) characterized the phase and graphitization of LG, regenerated graphite (RG), and commercial graphite (CG), showing identical characteristic diffraction peaks of graphite (Figure S18, Supporting Information). However, the lower intensity of the (002) diffraction peak in LG compared to RG and CG indicated poor graphitization caused by poor orientation of the graphite layer and the presence of impurities near the surface, consistent with Cryo-HRTEM results. In contrast, the (002) diffraction peak intensity of RG was nearly the same as CG, and exhibited sharper characteristics compared to LG, suggesting an enhanced level of graphitization after GMP regeneration. Additionally, the 2-theta (Figure S19, Supporting Information) of RG's (002) peak shifted slightly to a higher angle, indicating decreased lattice spacing and improved graphitization.

Raman spectra of LG, CG, and RG showed two typical peaks of graphite near 1350 and 1580 cm^{-1}, corresponding to the D-peak (disordered sp^3 hybridized carbon) and the G-peak (graphitized sp^2 hybridized carbon) of graphite, respectively (Figure 3b).[46,47] The ratio between the D-peak and G-peak of graphite materials serves as an indicator of the graphite defect and quality and the large ratio indicates more defects and impurities in the material. The I_D/I_G ratio for leached graphite was 0.36, whereas RG had a ratio of 0.15, similar to CG's 0.10. These results suggest that LG has more defects and impurities that disrupt the graphite structure, while RG has fewer defects and a higher degree of graphitization.

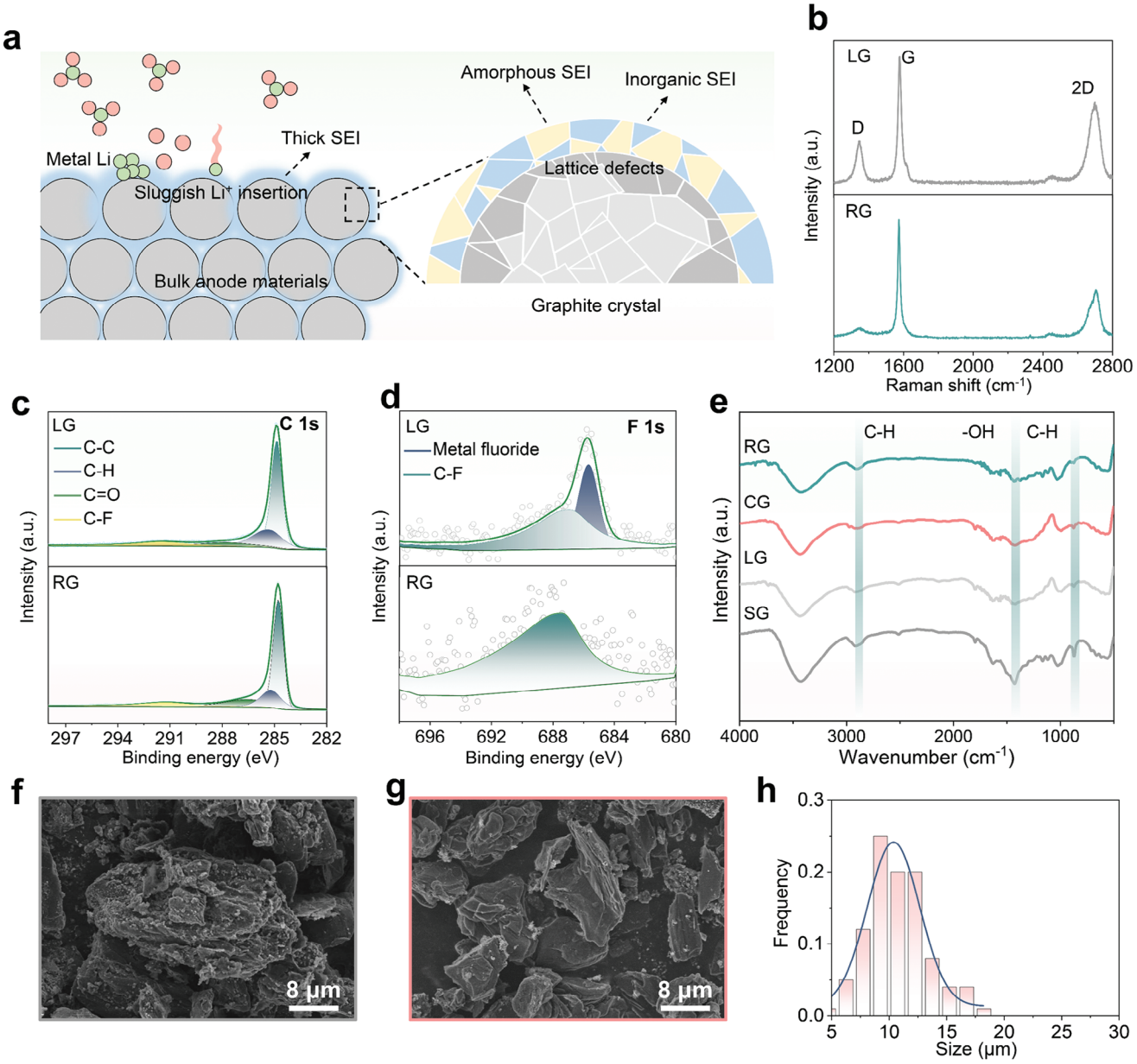

Figure 3. Characterization of the regenerated graphite anodes. a) Schematic illustration of spent graphite anode with a thick SEI. b) Statistical Raman spectra of LG and RG. XPS fitting results of c) C i1s and d) F 1s elements of LG and RG. e) FTIR spectrum of SG, LG, CG, and RG. SEM images of f) SG and g) RG and size distribution of h) RG particles.

XPS analysis was carried out to illustrate the changes in surface components. The XPS full spectrum of LG (Figure S20, Supporting Information) showed decreased elemental signals of F, O, and Li compared with SG (Figure 2i), indicating the removal of these components from residual organic binder or electrolyte. The peak fitting results of C 1s and F 1s (Figure 3c,d) revealed the disappearance of peaks associated with O—C—F, O—C—O, and the F element from $LiPF_6$ on the spent graphite surface after leaching. After GMP treatment, the peaks corresponding to the F and O elements in graphite were further attenuated, while the peaks of Li elements disappeared. The peak fitting indicates that the metal fluorides (Figure 3d) on the (RG) surface are removed, while the C—F bonds are retained, demonstrating the effective removal of thick SEI with inorganic LiF.

Infrared (IR) spectra of SG, LG, and RG exhibited weakened peaks corresponding to the —OH bending vibration at 1425.9 cm^{-1}, the C—H stretching vibration at 2909 cm^{-1}, and the C—H bending vibration at 869.0 cm^{-1} after leaching and regeneration of waste graphite (Figure 3e). These results confirm the effective removal of impurities, including the residual electrolyte, LiF, organic SEI components, and binder from the surface of spent graphite by leaching and GMP treatment.

TEM images demonstrated the graphite lattice after the regeneration. In Figure S21a (Supporting Information), the image

showed a clear lattice arrangement without obvious structural defects. Meanwhile, the graphite surface (Figure S21b,c, Supporting Information) showed a continuous and intact surface without amorphous coating, indicating the removal of SEI and demonstrating the effectiveness of plasma regeneration.

The morphology and particle size distribution of graphite particles were also examined. In the images of SG (Figure S22a–c, Supporting Information), the particles bonded with others closely, without contact, and clear graphite particles. Besides, the SG particles displayed a rough surface (Figure S23a, Supporting Information) with sizes ranging from 5 to 20 μm and an average of 13.5±0.27 μm (Figure S23b, Supporting Information), possibly due to the presence of binder and other impurities. Notably, some particles were visibly bonded together (Figure 3f). The leaching process reduced the particle size of LG and resulted in a narrower size distribution (Figure S24a, Supporting Information). However, the surface of LG remained rough (Figure S24b, Supporting Information). Unlike the regular morphology of CG (Figure S25a,b, Supporting Information), LG particles still exhibited partial bonding due to residual binder, resulting in uneven surface morphology (Figure S24b, Supporting Information). After GMP treatment, RG presented smoother surfaces and a more uniform particle size (Figure S26, Supporting Information; Figure 3g). The average particle size of RG was 10.4±0.22 μm (Figure 3h), closely resembling CG at 8.8±0.16 μm (Figure S25c, Supporting Information), further underscoring the effectiveness of this regeneration method.

In enlarged images, flocculent material emerged within the gaps of RG particles (Figure S27, Supporting Information). In contrast, no secondary impurities were observed in plasma-treated commercial graphite (Figure S28, Supporting Information). The flocculent material comprised spherical particles predominantly composed of carbon (Figure S29, Supporting Information). This carbonaceous material likely stems from the decomposition of residual carboxymethyl cellulose and its distribution in the interstices of the particles could improve the conductivity of the regenerated material. A trace amount (0.01% wt%) of fluorine (F) element was dispersed within the regenerated graphite, consistent with the presence of C—F bonding from XPS results, demonstrating that Li in LiF is reduced, and the residual F element bonds to C in graphite. These results indicate that regeneration through leaching and plasma treatment leads to notable refinement of spent graphite particles, characterized by a smooth surface morphology and a uniform particle size distribution. Furthermore, the post-regeneration state suggests successful elimination of binder and residual electrolyte from the graphite particles, resulting in morphology highly similar to commercial graphite.

2.3. Simulation of Plasma Regeneration Mechanism

To further explore the GMP treatment mechanism, simulations were conducted using commercial software Ansys HFSS and COMSOL Multiphysics to investigate electric and temperature fields around the samples.[48] Briefly, a model of the microwave oven (Figure S30, Supporting Information), including the waveguide and antenna, was constructed based on the actual size. Materials were sourced from the system materials within the software, with the exception of graphite sample electrical parameters, which were manually imported (conductivity: 1787 S m^{-1}, density: 2020 kg m^{-3}, dielectric constant: 18-J*0.12, thermal conductivity: 151 W $(m\ K)^{-1}$. The simulation parameters are detailed in the Supporting Information.

A crucible containing samples was placed in the oven, with stack powder samples simplified to a graphite sheet, aside from the particles on top (Figure S31, Supporting Information). The electric field trends in the oven under several conditions were simulated in Ansys HFSS by the finite element method at a solution frequency of 2.45 GHz, power of 1 W, and convergence condition less than 0.02. When the microwave oven was empty, the electric field strength was low and unevenly distributed (Figure S32, Supporting Information). With a crucible in the oven, the electrical field strength in the oven was nonuniform, with high strength points of less than 2,000 V m^{-1} located in the crucible (**Figure 4a**). In the absence of graphite with the same volume, the peak strength reached 3,000 V m^{-1}, and the field strength inside the crucible surrounding graphite was significantly higher than outside (Figure 4b,c). These trends indicate the formation of a strengthened electric field around the graphite particles in the microwave field, which may facilitate the ionization of the atmosphere to form plasma.[48,49]

Examining the discharge between irregular particles, the overall electric field showed no noticeable change (Figure S33, Supporting Information). However, the electric field distribution between particles indicated a relatively high field at the top of the graphite particles (Figure 4d), suggesting that the irregular morphology strengthens the electric field around the particles, potentially facilitating plasma formation on the particle surfaces (Figure 4e).

The temperature field was simulated using COMSOL multiphysics software to illustrate the thermal effect of plasma. The simulation model was based on the electric field simulation model used in the GMP experiment. For calculation efficiency, the model of waste graphite powder and nitrogen distribution was simplified. The inner wall and front panel of the microwave field adopted the finite conductivity boundary condition, and a solution frequency is 2.45 GHz. The heat generation of the particles was fitted by the following function.[50]

$$q(T) = A + BT = CT^2 \quad (1)$$

where A, B, and C are fitting values obtained from experiments on the decoupling of plasma and temperature: 24.11×10^8, 188.243×10^4 and -2.340×10^3, respectively. As shown in Figure 4f, there was a rapid heating rate within seconds, reaching and maintaining a temperature of 1400 K. The graphite materials could be heated to 1350 K in 2 s (Figure 4g; Figure S34, Supporting Information), demonstrating rapid heating caused by plasma.

Additionally, the temperature of the particles gradually increased from the inside to the outside with the highest temperature at the surface, close to the overall temperature value. The surface temperature rose above 1400 K (Figure 4h) when the thermal effect of plasma was applied. These findings show that when subjected to microwave, the electrical field surrounding the graphite materials is strengthened, especially around irregular particles. This strengthened electric field may contributed to

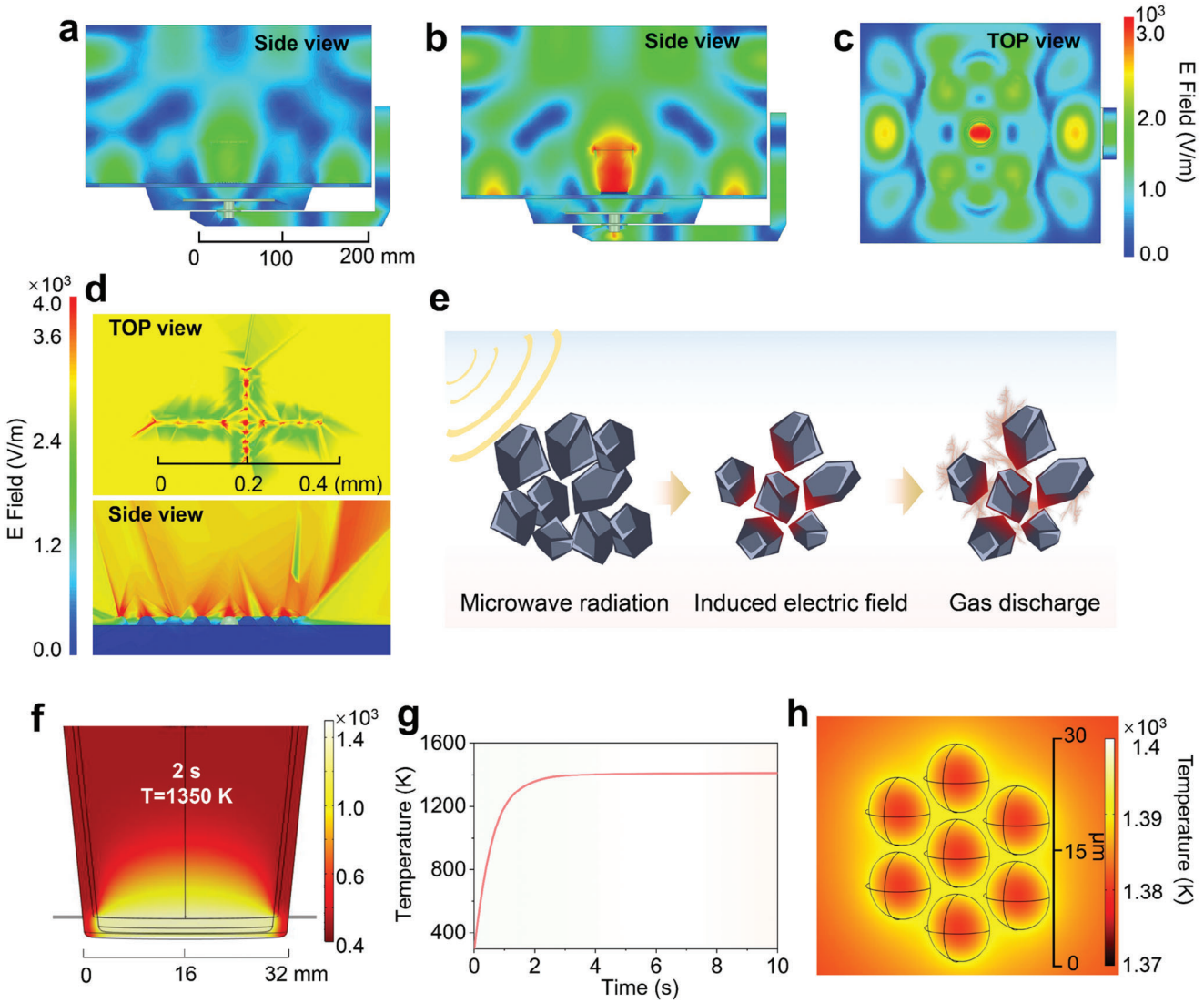

Figure 4. Simulation of plasma regeneration mechanism. The electrical field simulation of microwave reactor a) without graphite materials and b,c) with irregular graphite materials by HFSS. d) The electrical field of irregular graphite particles in detail. e) Schematic illustration of graphite self-induced plasma mechanism. f) The COMSOL Multiphysical simulation of the temperature of graphite materials in the 2 s. g) Plot of temperature as a function of time of the graphite materials. h) The COMSOL Multiphysical simulation of plasma heat-treatment of microscopic particles.

the plasma formation. To validate this assumption, an Ar atmosphere was used to generate plasma by the graphite-induced electric field due to its low ionization energy. An obvious plasma phenomenon formed rapidly (Figure S35, Supporting Information). Consequently, the SEI layer and other residues on the graphite surface were removed, and the crystal structure was repaired by graphite self-induced microwave plasma.

2.4. The Electrochemical Performance of Regenerated Graphite

The electrochemical performance of the RG anode was tested to evaluate the effectiveness of the GMP method. Cyclic voltammetry (CV) curves for the spent graphite anode are illustrated in Figure S36 (Supporting Information). Within the voltage range of 0–2.0 V, the SG demonstrated a notable irreversible reduction peak between 0.75 and 1.3 V and an additional irreversible reduction peak between 0.2 and 0.3 V. These observations align with the formation of the SEI layer due to electrolyte decomposition. Besides, it demonstrated a suddenly increased current in the second cycle, which may be due to the damage to the SG graphite structure. Compared with SG, the CV curve of the CG (Figure S37, Supporting Information) and RG (**Figure 5a**) revealed a similar irreversible reduction peak for SEI layer formation, mirroring the pattern observed in the SG. However, the reversible redox peaks of the regenerated anode are well-symmetrical and sharp, close to those of CG. The interfacial impedance values of the RG and CG anodes can be deduced from the Nyquist plots. All analyzed samples exhibited small semicircles and straight lines from high to low frequency (Figure 5b;

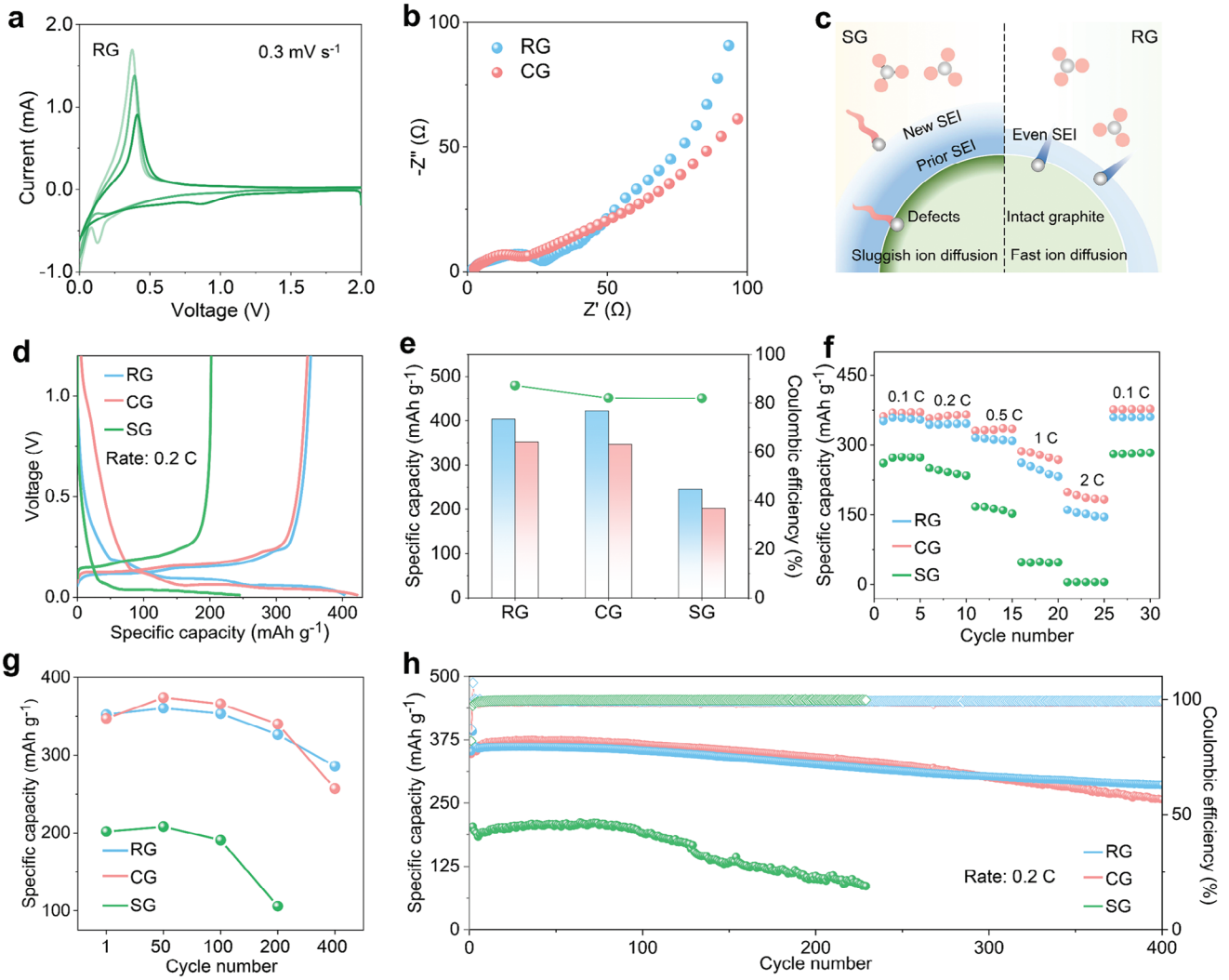

Figure 5. Evaluation of the electrochemical performance of regenerated graphite. a) The current voltage profiles of RG. b) The EIS of RG and CG after three cycles of activation. c) The schematic illustration of ion transportation of SG and RG. d) The initial cycle charge–discharge profile for RG, CG, and SG. e) The specific capacities at charge and discharge and the initial Coulombic efficiency of RG, CG, and SG. f) The rate capability of different graphite anodes. g) The specific charge capacities of RG, CG, and SG at different cycles. h) Cycling curve of RG, CG, and SG.

Figure S38 and S39, Supporting Information). The impedance results after three cycles of activation suggest excellent electrochemical properties for the RG (Figure 5b) than SG (Figure S38, Supporting Information). After 450 cycles, the RG exhibited lower impedance levels than CG (Figure S39, Supporting Information), consistent with its superior cycling stability.

These results indicate that the electrochemical properties of RG were restored after the removal of the residual thick SEI and structural defects, demonstrating faster ionic transportation than SG (Figure 5c). The initial voltage profiles of various anode materials at 0.2 C are shown in Figure 5d. SG exhibited a specific charge capacity of ≈201.8 mAh g^{-1}, while the RG had a specific capacity of ≈352.2 mAh g^{-1}, closely resembling the commercially available graphite anode of 347.1 mAh g^{-1}. The SEI layer formation during the charge and discharge process caused the capacity decline of charge capacity.[51] The decline of capacity (Figure 5e) is ≈46, 51, and 75 mAh g^{-1} in SG, RG, and CG, respectively. The regenerated anode exhibited an initial Coulombic efficiency of ≈87%, an improvement compared to the 81% observed in the spent graphite, and higher than the 82% of the CG. The initial capacity and efficiency of RG can be elevated to a level comparable to CG, emphasizing the potential of the GMP treatment.

The rate capability of different anode materials is shown in Figure 5f at 0.1, 0.2, 0.5, 1.0, and 2.0 C, respectively. The capacity of SG was lower than 10 mAh g^{-1} at a 2 C, below reuse criteria. In contrast, the capacity of the RG anode at different C-rates is close to the commercial levels. The specific capacities of the regenerated anode were 351.2, 343.7, 315.5, 261.9, and 145.4 mAh g^{-1} at 0.1, 0.2, 0.5, 1, and 2 C, respectively, close to those of the CG. In addition, the voltage profiles of graphite anodes at different rates are shown in Figure S40 (Supporting Information). The cycling stability of the spent graphite anode, as shown in Figure 5g,h, exhibited a capacity of 190.7 mAh g^{-1} after 100 cycles at 0.2 C, with slight fluctuation and fast decay (5.5%) during cycling. The

recycled anode provided a specific charge capacity of 285 mAh g^{-1} at 0.2 C after 400 cycles (Figure 5h), comparable to the electrochemical stability of CG (280 mAh g^{-1} after 400 cycles). The capacity retention of the recycled graphite during cycling was close to 81%, reaching the level of CG. These results demonstrate that GMP regeneration contributes to improved cycling stability of the graphite. The enhancement can be attributed to the restoration of the graphite structure, interface layer, and morphology, resulting in more durable performance. These findings imply the effective restoration of the electrochemical properties by GMP regeneration.

3. Conclusion

In summary, we have detailed the degradation mechanism of spent graphite using Cryo-TEM, revealing lattice defects and structure expansion near the surface, combined with a thick and uneven SEI layer. The degradation impairs the capacity and rate capability of graphite in subsequent utilization. To address this, we developed an innovative, scalable method using graphite self-induced microwave plasma following leaching. This method effectively removed the SEI layer and restored graphite lattices within seconds, regenerating spent graphite. The regenerated graphite exhibited a high degree of graphitization and a smooth surface free of residues. Multiphysics simulations explained the mechanism of the GMP method, showing that in the microwave field, the graphite materials induced a strong electric field, ionizing the air to form plasma around them. This plasma heated the graphite surface to ≈1400 K within 3 s, maintaining a high temperature to remove impurities and restore the crystal structure. Post-regeneration, the graphite achieved a specific capacity of 352.2 mAh g^{-1} at 0.2 C and a capacity retention of 81% after 400 cycles, comparable to commercial graphite. This demonstrates the effectiveness of the GMP method in regenerating spent graphite anodes for high-performance applications.

4. Experimental Section

Experimental Process: Retired $LiCoO_2$ batteries were obtained from battery companies. The spent batteries were placed inside a glove box filled with argon for disassembly to obtain battery materials, primarily spent graphite (SG) sheets from the anode. The SG sheets were placed in water and ethanol (volume ratio 5:1) and ultrasonicated for 3 min. The mixed solution was then centrifuged at 5000 rpm for 3 min to remove the supernatant and obtain the mixture containing graphite. The obtained graphite mixture was dried in an oven at 80 °C for 12 h to yield leached graphite (LG). The LG powder was subsequently placed in a quartz vessel and treated with graphite self-induced microwave plasma for 30 s under a nitrogen atmosphere to produce regenerated graphite.

Characterization: Scanning electron microscopy (SEM) was conducted using a Zeiss Merlin high-resolution SEM. X-ray diffraction (XRD) analysis was conducted with a Bruker D8 Advance instrument utilizing Cu Kα radiation (XRD, λ = 0.15406 nm). X-ray photoelectron spectroscopy (XPS) was performed on an Escalab 250Xi* with Al Kα radiation (1486.6 eV) as the X-ray source. Raman spectroscopy was performed with an inVia Reflex Laser Raman Spectrometer (λ = 532 nm). EDS mapping was recorded using a Quantax 200 Xflash system. TEM images were captured using the Cryo-HRTEM (FEI Krios G3i) technique, employing ultra-low-dose and low-temperature TEM technology. The microscope was equipped with a Folcon 3 camera featuring direct electron detection and consistently maintained at a temperature near −192 °C throughout the holder.

Supporting Information

Supporting Information is available from the Wiley Online Library or from the author.

Acknowledgements

This work is partially supported by the National Key Research and Development Program of China (2022YFB3803502), and the National Natural Science Foundation of China (52103076). C.C. acknowledges the support from Case Western Reserve University.

Conflict of Interest

The authors declare no conflict of interest.

Author Contributions

G.X. conceived the idea. G.X. and M.S. designed the experiments. M.S., X.Z., and C.D. prepared materials, assembled cells, and performed all other measurements. S.X. and Q.Z. performed numerical simulations, and Y.X. tested the FTIR experiments. Q.Z. measured SEM. T.Z. assisted revised the manuscript. G.X., Y.C., C.C., and M.S. wrote and edited the manuscript. All the authors commented on the manuscript.

Data Availability Statement

The data that support the findings of this study are available from the corresponding author upon reasonable request.

Keywords

battery recycling, degradation mechanism, graphite anode, plasma recycling, spent lithium-ion batteries

Received: July 5, 2024
Revised: August 7, 2024
Published online:

[1] L. X. Yuan, Z. H. Wang, W. X. Zhang, X. L. Hu, J. T. Chen, Y. H. Huang, J. B. Goodenough, *Energy Environ. Sci.* **2011**, *4*, 269.
[2] H. Li, Z. Wang, L. Chen, X. Huang, *Adv. Mater.* **2009**, *21*, 4593.
[3] J. B. Goodenough, Y. Kim, *Chem. Mater.* **2010**, *22*, 587.
[4] A. Manthiram, *Nat. Commun.* **2020**, *11*, 1550.
[5] X. Xiao, L. Wang, Y. Wu, Y. Song, Z. Chen, X. He, *Energy Environ. Sci.* **2023**, *16*, 2856.
[6] J. J. Roy, N. Zaiden, M. P. Do, B. Cao, M. Srinivasan, *Joule* **2023**, *7*, 450.
[7] J. Lin, X. Zhang, E. Fan, R. Chen, F. Wu, L. Li, *Energy Environ. Sci.* **2023**, *16*, 745.
[8] K. Meng, G. Xu, X. Peng, K. Youcef-Toumi, J. Li, *Resour. Conserv. Recycl.* **2022**, *182*, 106207.
[9] J. Xiao, C. Jiang, B. Wang, *Batteries* **2023**, *9*, 57.
[10] B. Wang, X. Xiao, J. Li, M. Zhang, M. Jiao, Z. Zheng, T. Li, Q. Zhang, X. Zhang, G. Zhou, *Proc. Natl. Acad. Sci* **2023**, *120*, 2317174120.
[11] P. Xu, D. H. S. Tan, B. Jiao, H. Gao, X. Yu, Z. Chen, *Adv. Funct. Mater.* **2023**, *33*, 2213168.

[12] V. Gupta, X. Yu, H. Gao, C. Brooks, W. Li, Z. Chen, *Adv. Energy Mater.* **2023**, *13*, 2203093.
[13] J. Yu, J. Li, S. Zhang, F. Wei, Y. Liu, J. Li, *Proc. Natl. Acad. Sci* **2023**, *120*, 2217698120.
[14] Y. Yang, E. G. Okonkwo, G. Huang, S. Xu, W. Sun, Y. He, *Energy Storage Mater.* **2021**, *36*, 186.
[15] G. Harper, R. Sommerville, E. Kendrick, L. Driscoll, P. Slater, R. Stolkin, A. Walton, P. Christensen, O. Heidrich, S. Lambert, A. Abbott, K. Ryder, L. Gaines, P. Anderson, *Nature* **2019**, *575*, 75.
[16] Z. Huang, Z. Deng, Y. Zhong, M. Xu, S. Li, X. Liu, Y. Zhou, K. Huang, Y. Shen, Y. Huang, *Carbon Energy* **2022**, *4*, 1107.
[17] L. Jin, C. Shen, Q. Wu, A. Shellikeri, J. Zheng, C. Zhang, J. P. Zheng, *Adv. Sci.* **2021**, *8*, 2005031.
[18] C. Dang, A. S. Helal, L. Zhu, G. Xu, M. Zhu, *Nano Res. Energy* **2023**, *2*, 9120059.
[19] X. Chang, M. Fan, B. Yuan, C. F. Gu, W. H. He, C. Li, X.-X. Feng, S. Xin, Q. Meng, L.-J. Wan, Y.-G. Guo, *Angew. Chem., Int. Ed.* **2023**, *62*, 202310435.
[20] J. Xu, Y. Jin, K. Liu, N. Lyu, Z. Zhang, B. Sun, Q. Jin, H. Lu, H. Tian, X. Guo, D. Shanmukaraj, H. Wu, M. Li, M. Armand, G. Wang, *Sci. Adv.* **2022**, *8*, eabq7948.
[21] Z. Liang, C. Cai, G. Peng, J. Hu, H. Hou, B. Liu, S. Liang, K. Xiao, S. Yuan, J. Yang, *ACS Sustainable Chem. Eng.* **2021**, *9*, 5750.
[22] J. Yang, E. Fan, J. Lin, F. Arshad, X. Zhang, H. Wang, F. Wu, R. Chen, L. Li, *ACS Appl. Energy Mater.* **2021**, *4*, 6261.
[23] H. Tian, M. Graczyk-Zajac, A. Kessler, A. Weidenkaff, R. Riedel, *Adv. Mater.* **2024**, *36*, 2308494.
[24] Y. Qiao, H. Zhao, Y. Shen, L. Li, Z. Rao, G. Shao, Y. Lei, *EcoMat* **2023**, *5*, e12321.
[25] J. Wang, J. Ma, K. Jia, Z. Liang, G. Ji, Y. Zhao, B. Li, G. Zhou, H. M. Cheng, *ACS Energy Lett.* **2022**, *7*, 2816 .
[26] W. Fan, J. Zhang, R. Ma, Y. Chen, C. Wang, *J. Electroanal. Chem.* **2022**, *908*, 116087 .
[27] Z. Cheng, Z. Luo, H. Zhang, W. Zhang, W. Gao, Y. Zhang, L. Qie, Y. Yao, Y. Huang, K. K. Fu, *Carbon Energy* **2023**, *6*, e395.
[28] R. Shi, N. Zheng, H. Ji, M. Zhang, X. Xiao, J. Ma, W. Chen, J. Wang, H. M. Cheng, G. Zhou, *Adv. Mater.* **2024**, *36*, 2311553.
[29] Y. Zhao, Y. Kang, M. Fan, T. Li, J. Wozny, Y. Zhou, X. Wang, Y.-L. Chueh, Z. Liang, G. Zhou, J. Wang, N. Tavajohi, F. Kang, B. Li, *Energy Storage Mater.* **2022**, *45*, 1092.
[30] H. Zhang, Y. Ji, Y. Yao, L. Qie, Z. Cheng, Z. Ma, X. Qian, R. Yang, C. Li, Y. Guo, Y. Yuan, H. Xiao, H. Yang, J. Ma, J. Lu, Y. Huang, *Energy Environ. Sci.* **2023**, *16*, 2561.
[31] W. Chen, R. V. Salvatierra, J. T. Li, C. Kittrell, J. L. Beckham, K. M. Wyss, N. La, P. E. Savas, C. Ge, P. A. Advincula, P. Scotland, L. Eddy, B. Deng, Z. Yuan, J. M. Tour, *Adv. Mater.* **2022**, *35*, 2207303.
[32] T. Li, L. Tao, L. Xu, T. Meng, B. C. Clifford, S. Li, X. Zhao, J. Rao, F. Lin, L. Hu, *Adv. Funct. Mater.* **2023**, *33*, 2302951.
[33] G. Xu, H. Jiang, M. Stapelberg, J. Zhou, M. Liu, Q. J. Li, Y. Cao, R. Gao, M. Cai, J. Qiao, M. S. Galanek, W. Fan, W. Xue, B. Marelli, M. Zhu, J. Li, *Environ. Sci. Technol.* **2021**, *55*, 6239.
[34] W. Bao, W. Yao, Y. Li, B. Sayahpour, B. Han, G. Raghavendran, R. Shimizu, A. Cronk, M. Zhang, W. Li, Y. S. Meng, *Energy Environ. Sci.* **2024**, *17*, 4263.
[35] M. Abdollahifar, S. Doose, H. Cavers, A. Kwade, *Adv. Mater. Technol.* **2023**, *8*, 2200368.
[36] B. Han, Y. Zou, G. Xu, S. Hu, Y. Kang, Y. Qian, J. Wu, X. Ma, J. Yao, T. Li, Z. Zhang, H. Meng, H. Wang, Y. Deng, J. Li, M. Gu, *Energy Environ. Sci.* **2021**, *14*, 4882.
[37] PubChem. Lithium fluoride, accessed January 9 2024, https://pubchem.ncbi.nlm.nih.gov/compound/224478.
[38] S. J. An, J. Li, C. Daniel, D. Mohanty, S. Nagpure, D. L. Wood, *Carbon* **2016**, *105*, 52.
[39] V. A. Agubra, J. W. Fergus, *J. Power Sources* **2014**, *268*, 153.
[40] W. Cai, Y. X. Yao, G. L. Zhu, C. Yan, L. L. Jiang, C. He, J. Q. Huang, Q. Zhang, *Chem. Soc. Rev.* **2020**, *49*, 3806 .
[41] Z. Li, J. Huang, B. Yann Liaw, V. Metzler, J. Zhang, *J. Power Sources* **2014**, *254*, 168.
[42] T. Liu, L. Lin, X. Bi, L. Tian, K. Yang, J. Liu, M. Li, Z. Chen, J. Lu, K. Amine, K. Xu, F. Pan, *Nature Nanotech* **2019**, *14*, 50.
[43] M. Shan, C. Dang, K. Meng, Y. Cao, X. Zhu, J. Zhang, G. Xu, M. Zhu, *Mater. Today* **2024**, *73*, 130.
[44] T. Gao, Y. Han, D. Fraggedakis, S. Das, T. Zhou, C. N. Yeh, S. Xu, W. C. Chueh, J. Li, M. Z. Bazant, *Joule* **2021**, *5*, 393.
[45] J. Lu, Y. Zhao, Y. Kang, C. Li, Y. Liu, L. Wang, H. Du, M. Fan, Y. Zhou, J. Wozny, T. Li, N. Tavajohi, F. Kang, B. Li, *Carbon Energy* **2023**, *5*, e282.
[46] F. Tuinstra, J. L. Koenig, *J. Chem. Phys.* **2003**, *53*, 1126.
[47] X. Zhu, F. Guo, Q. Yang, H. Mi, C. Yang, J. Qiu, *J. Power Sources* **2021**, *506*, 230224.
[48] L. Li, M. Yu, Z. Zhang, L. Zhang, Y. Zhang, Z. Zhao, K. Cao, J. Sun, D. Cai, *J. Environ. Chem. Eng.* **2023**, *11*, 109728.
[49] F. Zhang, X. Zhang, Z. Song, X. Li, X. Zhao, J. Sun, Y. Mao, X. Wang, W. Wang, *Fuel* **2023**, *331*, 125914.
[50] L. Li, Z. Zhao, D. Cai, M. Yu, Z. Zhang, K. Cao, J. Sun, Q. Zhang, G. Zou, C. Wang, *J. Energy Inst.* **2023**, *108*, 101234.
[51] D. Rehnlund, Z. Wang, L. Nyholm, *Adv. Mater.* **2022**, *34*, 2108827.